Journal of Alloys and Compounds 509 (2011) 5740–5747

Contents lists available at ScienceDirect

Journal of Alloys and Compounds

journal homepage: www.elsevier.com/locate/jallcom

# Experimental investigation of phase equilibria in the Co–W–V ternary system

Xingjun Liu, Yihong Zhu, Yan Yu, Cuiping Wang*

*Department of Materials Science and Engineering, College of Materials, and Research Center of Materials Design and Application, Xiamen University, No. 422 Siming South Road, Xiamen 361005, Fujian, PR China*

ARTICLE INFO

*Article history:*
Received 5 September 2010
Received in revised form
30 December 2010
Accepted 4 January 2011
Available online 1 March 2011

*Keywords:*
Metals and alloys
Phase diagrams
Microstructure
X-ray diffraction

ABSTRACT

The phase equilibria in the Co–W–V ternary system were experimentally investigated by optical microscopy (OM), electron probe microanalysis (EPMA) and X-ray diffraction (XRD) on the equilibrated alloys. Three isothermal sections of the Co–W–V ternary system at 1100 °C, 1200 °C and 1300 °C were determined, and no ternary compound was found in this system. In addition, a novel phenomena induced by the liquid phase separation in the Co–W–V alloys was firstly discovered, suggesting that a stable liquid miscibility gap exists in the Co–W–V ternary system. The newly determined phase equilibria and firstly discovered phase separation phenomena in the Co–W–V system will provide important information for the development of Co–W based alloys.



## 1. Introduction

Co–W based cemented carbides are important materials for the applications of metal cutting, milling, turning or rock drilling [1]. For the purpose of manufacturing cemented carbides with small WC grains, certain carbides, such as VC (the most efficient inhibitor), are usually added to inhibit grain growth during sintering [2–4]. Therefore, the Co–W–V ternary system is one of the important subsystems of the Co–W based cemented carbide system. In addition, the Co–W based alloys are widely used as high-speed steels [5,6]. For the advanced development of Co–W based alloys, accurate phase equilibria in the Co–W–V ternary system is especially required. However, until now, no information about the phase equilibria in this system is available in the literature. Therefore, it is important and necessary to comprehensively determine the phase equilibria in the Co–W–V ternary system.

Three binary systems Co–W, Co–V and W–V, constituting the Co–W–V ternary system, is shown in Fig. 1. In the Co–W binary system [7], two intermediate phases of the $Co_3W$ and $Co_7W_6$ form through peritectoid reaction at 1093 °C and peritectic reaction at 1689 °C, respectively. The Co–V binary system was reviewed by Smith [8], where there are four intermediate phases ($Co_3V$ (fcc), $Co_3V$ (hex), $CoV_3$ and σ-$Co_2V_3$). The W–V system [9] is a simple system without any intermediate phase. All the stable solid phases in the three binary systems are summarized in Table 1.

The purpose of the present work is to experimentally determine the phase equilibria in the Co–W–V ternary system at 1100 °C, 1200 °C and 1300 °C by using optical microscopy (OM), electron probe microanalysis (EPMA) and X-ray diffraction (XRD), which will provide a better understanding of microstructures of promising alloys in the Co–W–V ternary system for practical applications.

## 2. Experimental procedure

High-purity cobalt (99.9 wt.%), tungsten (99.9 wt.%) and vanadium (99.9 wt.%) were used as starting materials. Bulk alloy buttons were prepared from pure elements by arc melting under a high purity argon atmosphere using a non-consumable tungsten electrode. The ingots were melted eight times in order to achieve their homogeneity. The sample weight was around 20 g and the weight loss during melting was generally less than 0.20% of the sample weight. Afterwards, the ingots were cut into small pieces for heat treatment and further observations.

Plate-shaped specimens were wrapped in W foil in order to prevent direct contact with the quartz ampoule, and put into quartz ampoule evacuated and backfilled with argon gas. The specimens were annealed at 1100 °C, 1200 °C and 1300 °C for 5 weeks, 3 weeks and 1 week, respectively. After the heat treatment, the specimens were quenched into ice water.

After standard metallographic preparation, the microstructural observations were carried out by optical microscopy (OM). The equilibrium compositions of the equilibrated alloys were examined by electron probe microanalysis (EPMA) (JXA-8100R, JEOL, Japan). Pure elements were used as standards and the measurements were carried out at 20.0 kV. The X-ray diffraction (XRD) was used to identify the crystal structure of the constituent phases. The XRD measurement was carried out on a Phillips Panalytical X-pert diffractometer using CuKα radiation at 40.0 kV and 30 mA. The data were collected in the range of 2θ from 30° to 90° at a step with of 0.0167°.

* Corresponding author. Tel.: +86 592 2180606; fax: +86 592 2187966.
*E-mail address:* wangcp@xmu.edu.cn (C. Wang).

0925-8388/$ – see front matter © 2011 Elsevier B.V. All rights reserved.
doi:10.1016/j.jallcom.2011.01.212

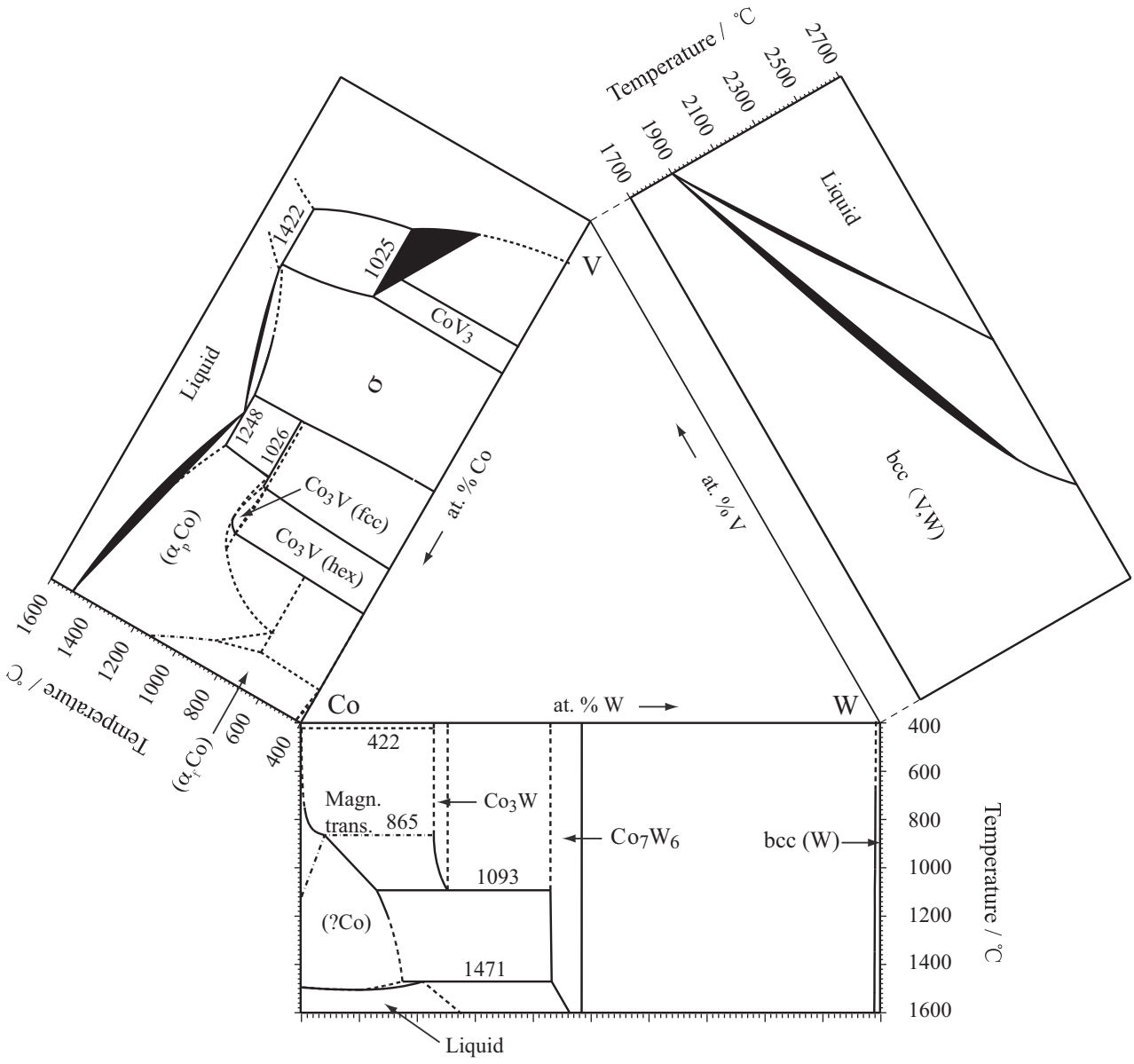


**Fig. 1.** Binary phase diagrams constituting the Co–W–V ternary system.

**Table 1**
The stable solid phases in the three binary systems.

| System | Phase | Pearson's symbol | Prototype | Space group | Strukturbericht | References |
|---|---|---|---|---|---|---|
| Co–W | εCo | *hP*2 | Mg | $P6_3/mmc$ | *A*3 | [7] |
| | αCo | *cF*4 | Cu | *Fm*-3*m* | *A*1 | [7] |
| | $Co_3W$ | *hP*8 | $Ni_3Sn$ | $P6_3/mmc$ | $D0_{19}$ | [7] |
| | $Co_7W_6$ | *hR*13 | $Fe_7W_6$ | *R*-3*m* | $D8_5$ | [7] |
| | bcc (W) | *cI*2 | W | *Im*-3*m* | *A*2 | [7] |
| Co–V | αCo | *cF*4 | Cu | *Fm*-3*m* | *A*1 | [8] |
| | εCo | *hP*2 | Mg | $P6_3/mmc$ | *A*3 | [8] |
| | $Co_3V$ (hex) | *hP*24 | $Co_3V$ | *P*-6*m*2 | – | [8] |
| | $Co_3V$ (fcc) | *cP*4 | $AuCu_3$ | *Pm*-3*m* | $L1_2$ | [8] |
| | σ | *tP*30 | σCrFe | $P4_2/mnm$ | $D8_b$ | [8] |
| | $CoV_3$ | *cP*8 | $Cr_3Si$ | *Pm*-3*n* | *A*15 | [8] |
| | bcc (V) | *cI*2 | W | *Im*-3*m* | *A*2 | [8] |
| W–V | bcc (V, W) | *cI*2 | W | *Im*-3*m* | *A*2 | [9] |

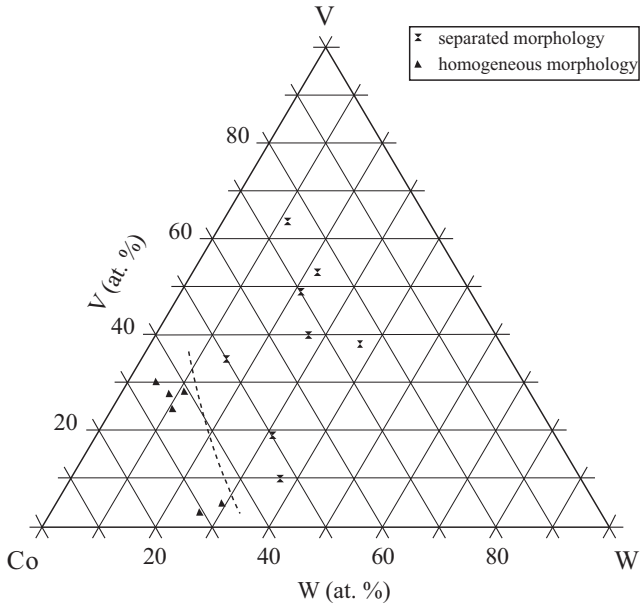


**Fig. 2.** Locations of the alloys with separated (⧗) and homogeneous (▲) morphology in the Co–W–V ternary system.

## 3. Results and discussion

### 3.1. Liquid phase separation phenomena

The as-cast $Co_{65}W_5V_{30}$, $Co_{65}W_{10.5}V_{24.5}$, $Co_{66}W_{29}V_5$, $Co_{71}W_{26}V_3$, $Co_{64}W_{8.5}V_{27.5}$ and $Co_{61}W_{11}V_{28}$ (at. %) alloys show the homogeneous microscopic morphologies, while the as-cast $Co_{25}W_{11.5}V_{63.5}$, $Co_{25}W_{22}V_{53}$, $Co_{30}W_{21}V_{49}$, $Co_{50}W_{15}V_{35}$, $Co_{53}W_{37}V_{10}$, $Co_{50}W_{31}V_{19}$, $Co_{50}W_{15}V_{39}$ and $Co_{33}W_{27}V_{40}$ (at. %) alloys exhibit the top–bottom separated microscopic morphologies, which are caused by the liquid phase separation. The location of the above-mentioned Co–W–V alloys is plotted in Fig. 2, where types of microscopic morphologies were marked by different symbols and the liquid phase separation region may be at the right of the dashed line. Typical separated microstructure of the $Co_{53}W_{37}V_{10}$ (at. %) alloy and its magnification part are shown in Fig. 3. The top–bottom separated microscopic morphology attributes to the density difference of the Co-rich and W-rich liquids during the solidification process under gravity condition, thus an horizontal boundary between the Co-rich and W-rich layers can be clearly observed (Fig. 3(a)). In addition, the individual phases of the $Co_{53}W_{37}V_{10}$ (at. %) alloy (Fig. 3(b)) were identified by the EPMA, and their compositions are presented in Table 2.

Recently, great attention has been paid to the liquid phase separation and its effect on the formation of composite materials. For instance, a variety of the Cu–Fe based composite materials with core-type structures or pencil-like core macroscopic morphologies were produced by different methods [10–12]. In particular, pencil-like buck composite materials with the core macroscopic morphologies were successfully fabricated from liquid immiscible Cu–Fe based alloys [12] using the conventional casting process, indicating that it is possible to obtain the Co–W based pencil-like buck composite materials. Thus, such kind of Co–W based composite material will show potential application in cemented carbide industry.

### 3.2. Microstructure and phase equilibria

Typical BSE (back-scattered electron) image of the $Co_{53}W_{37}V_{10}$ (at. %) alloy (separated morphology) annealed at 1300 °C for 1 week, is shown in Fig. 4, where attractive voids formed near the Co-rich layer/$Co_7W_6$ interface. The formation of these voids maybe induced by the different diffusion flux of Co atoms and W atoms at 1300 °C. Comparing the as-cast microstructure (Fig. 3(b)) with the equilib-

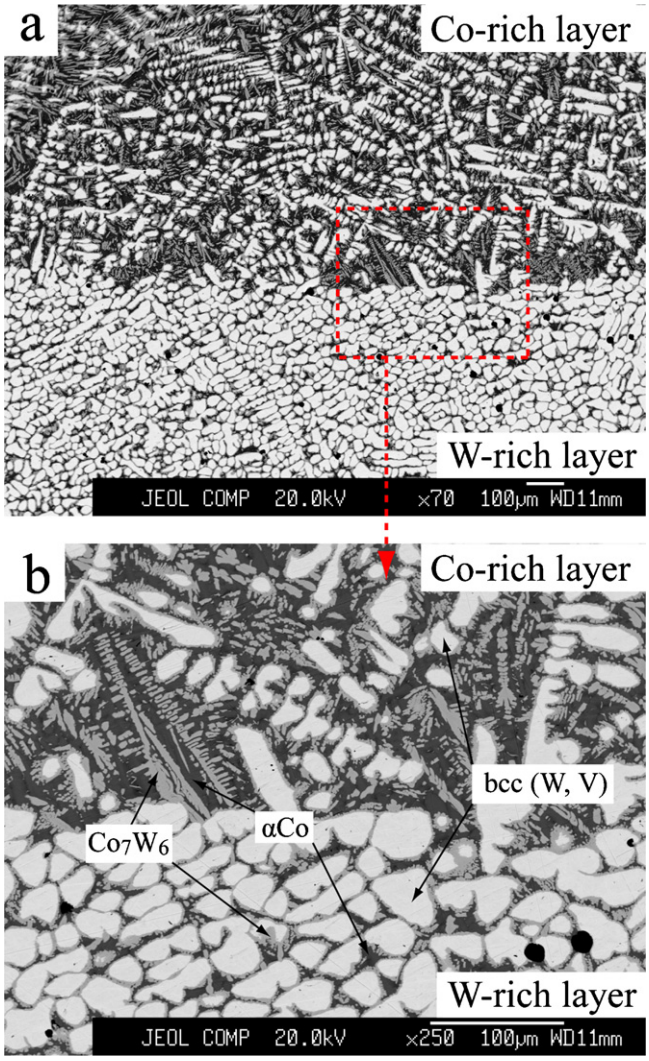


**Fig. 3.** Typical separated microstructure (a) of the as-cast $Co_{53}W_{37}V_{10}$ (at. %) alloy and its magnification part (b).

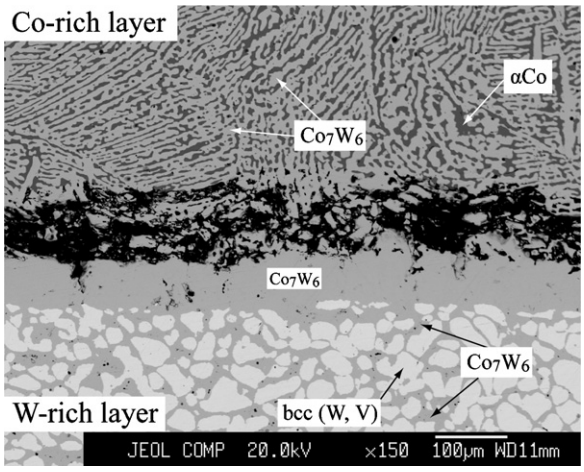


**Fig. 4.** Typical BSE image of the $Co_{53}W_{37}V_{10}$ (at. %) alloy (separated morphology) annealed at 1300 °C for 1 week.

**Table 2**
The composition of the individual phases in the as-cast $Co_{53}W_{37}V_{10}$ (at. %) alloy.

| As-cast $Co_{53}W_{37}V_{10}$ (at. %) alloy | Composition (at. %) | | | | | | | | |
|---|---|---|---|---|---|---|---|---|---|
| | bcc (W, V) | | | $Co_7W_6$ | | | αCo | | |
| | Co | W | V | Co | W | V | Co | W | V |
| Co-rich layer | 1.5 | 95.5 | 3.0 | 56.7 | 35.5 | 7.8 | 79.8 | 10.2 | 10.0 |
| W-rich layer | 1.5 | 95.6 | 2.9 | 56.1 | 38.5 | 5.4 | 78.7 | 10.0 | 11.3 |

**Table 3**
Average composition of each layer of the $Co_{53}W_{37}V_{10}$ (at. %) alloy in different states.

| $Co_{53}W_{37}V_{10}$ (at. %) alloy | Average composition (at. %) | | | | | |
|---|---|---|---|---|---|---|
| | As-cast | | | Annealed at 1300 °C | | |
| | Co | W | V | Co | W | V |
| Co-rich layer | 57.0 | 31.8 | 11.2 | 61.6 | 26.7 | 11.7 |
| W-rich layer | 33.9 | 57.5 | 8.6 | 24.3 | 68.6 | 7.1 |

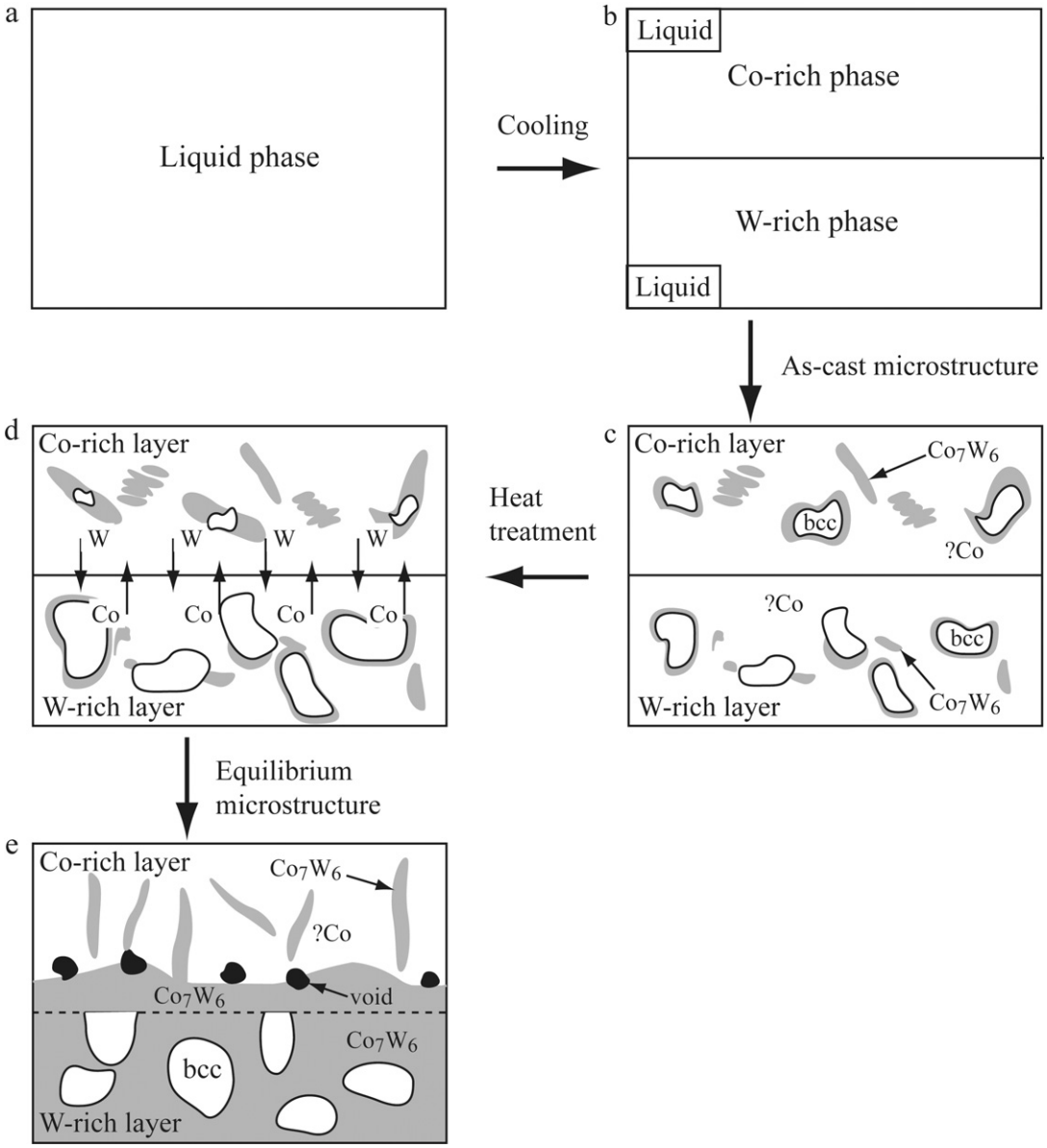


**Fig. 5.** Microstructural evolution of the $Co_{53}W_{37}V_{10}$ (at. %) alloy during the solidification and annealing process: (a) totally melting; (b) cooling a little; (c) as-cast state; (d) annealing for a short time; and (e) in equilibrium state.

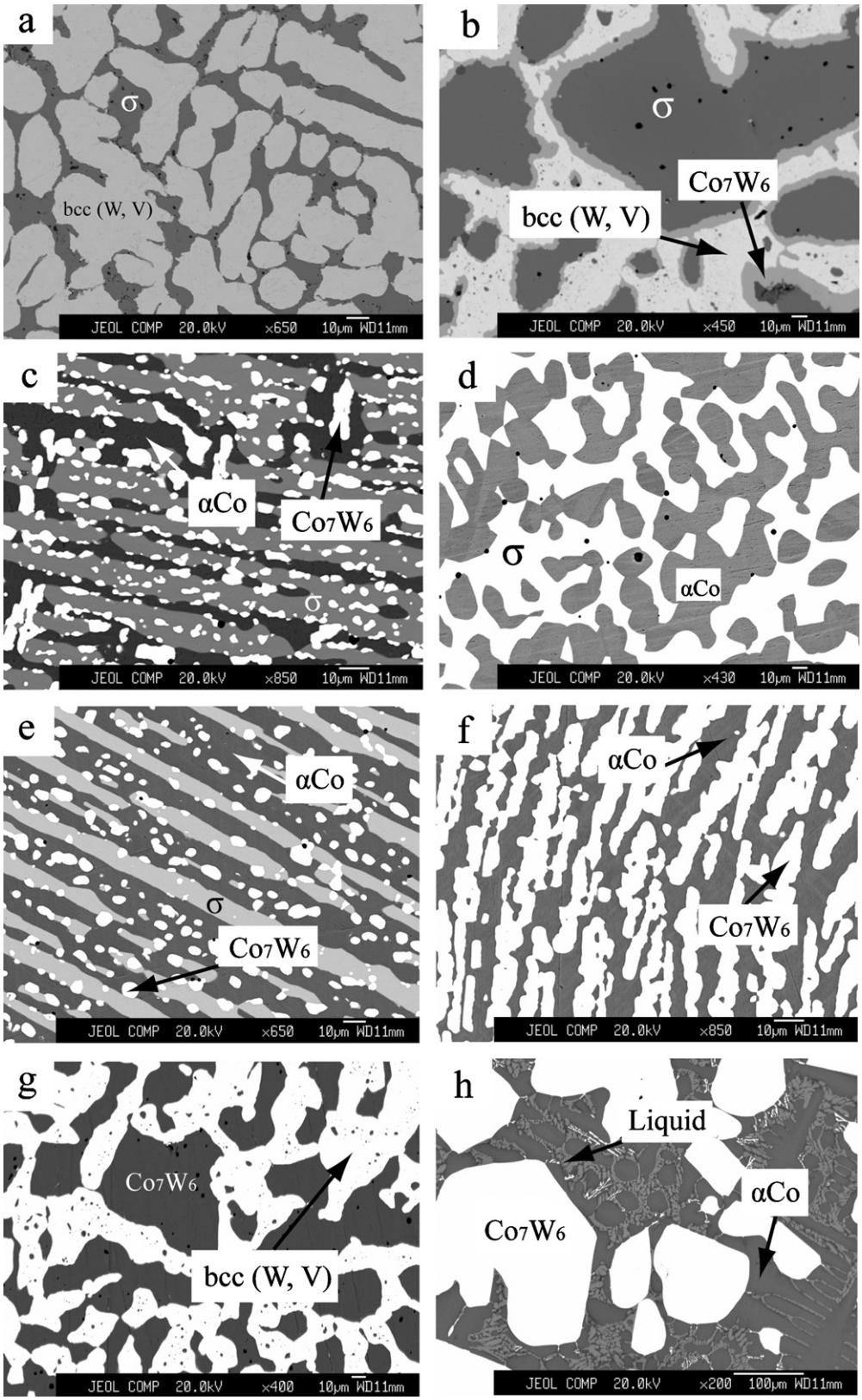


**Fig. 6.** Typical ternary BSE images obtained from: (a) the W-rich layer of the $Co_{25}W_{37}V_{38}$ (at. %) alloy annealed at 1100 °C for 5 weeks; (b) the Co-rich layer of the $Co_{50}W_{15}V_{35}$ (at. %) alloy annealed at 1100 °C for 5 weeks; (c) the $Co_{61}W_{11}V_{28}$ (at. %) alloy annealed at 1100 °C for 5 weeks; (d) the $Co_{65}W_5V_{30}$ (at. %) alloy annealed at 1200 °C for 3 weeks; (e) the $Co_{64}W_{8.5}V_{27.5}$ (at. %) alloy annealed at 1200 °C for 3 weeks; (f) the $Co_{71}W_{26}V_3$ (at. %) alloy annealed at 1300 °C for 1 week; (g) the W-rich layer of the $Co_{50}W_{15}V_{35}$ (at. %) alloy annealed at 1300 °C for 1 week and (h) the $Co_{65}W_{10.5}V_{24.5}$ (at. %) alloy annealed at 1300 °C for 1 week.

rium microstructure (Fig. 4) of the $Co_{53}W_{37}V_{10}$ (at. %) alloy, both the bcc (W, V) phase in the Co-rich layer and the αCo phase in W-rich layer (Fig. 3(b)) disappear after annealing at 1300 °C for one week, which suggests that the above-mentioned phases are not the equilibrium phases. In order to show the microstructural evolution of the $Co_{53}W_{37}V_{10}$ (at. %) alloy during the solidification and annealing process, hypothetically, a sketch scheme, representing the solidification process and annealing process, was presented in Fig. 5. In particular, as presented in Fig. 5(d), W atoms diffuse from the Co-rich layer to the W-rich layer, while Co atoms show an opposite diffusion path. The above diffusion paths have been confirmed by the composition changes listed in Table 3, which shows the average solubility of Co atom in the Co-rich layer increases and W atom in this layer decreases after annealing at 1300 °C.

Several BSE images of the typical ternary Co–W–V alloys are shown in Fig. 6(a)–(h). Phase identification was based on the equilibrium composition as measured by EPMA and XRD results. In the W-rich layer of the $Co_{25}W_{37}V_{38}$ (at. %) alloy quenched from 1100 °C, the two-phase equilibrium microstructure (σ + bcc (W, V)) was observed (Fig. 6(a)) and substantiated by the XRD result, as shown in Fig. 7(a), where the characteristic peaks of the σ and bcc (W, V) phases are confirmed and well marked by different symbols. The three-phase equilibrium of the $Co_7W_6$ + bcc (W, V) + σ was identified in the Co-rich layer of the $Co_{50}W_{15}V_{35}$ (at. %) alloy annealed at 1100 °C, and is shown in Fig. 6(b), where the $Co_7W_6$ phase appears between the σ and bcc (W, V) phases, suggesting that the $Co_7W_6$ phase may form though the peritectoid reaction of the σ + bcc (W, V) → $Co_7W_6$. Fig. 6(c) shows the three-phase equilibrium of the αCo + $Co_7W_6$ + σ in the $Co_{61}W_{11}V_{28}$ (at. %) alloy equilibrated at 1100 °C. Two images of the $Co_{65}W_5V_{30}$ (at. %) and $Co_{64}W_{8.5}V_{27.5}$ (at. %) alloys annealed at 1200 °C were shown in Fig. 6(d) and (e), where two-phase equilibrium of the αCo + σ and three-phase equilibrium of the αCo + $Co_7W_6$ + σ can be clearly observed, respectively. In the $Co_{71}W_{26}V_3$ (at. %) alloy quenched from 1300 °C, two phases namely αCo and $Co_7W_6$ were identified by EPMA, as shown in Fig. 6(f), where the $Co_7W_6$ phase irregularly distributes in the matrix of the αCo phase. Fig. 6(g) shows the two-phase microstructure of the $Co_7W_6$ + bcc (W, V) of the W-rich layer of $Co_{50}W_{15}V_{35}$ (at. %) alloy annealed at 1300 °C, and the XRD result is shown in Fig. 7(b), where the characteristic peaks of the $Co_7W_6$ and bcc (W, V) phases are well distinguished by different symbols. In addition, the $Co_{65}W_{10.5}V_{24.5}$ (at. %) alloy annealed at 1300 °C is located in the three-phase region of the αCo + $Co_7W_6$ + liquid, as characterized in Fig. 6(h), where the liquid phase tends to surround the αCo phase, indicating that the eutectic reaction of the αCo + σ ↔ liquid occurs.

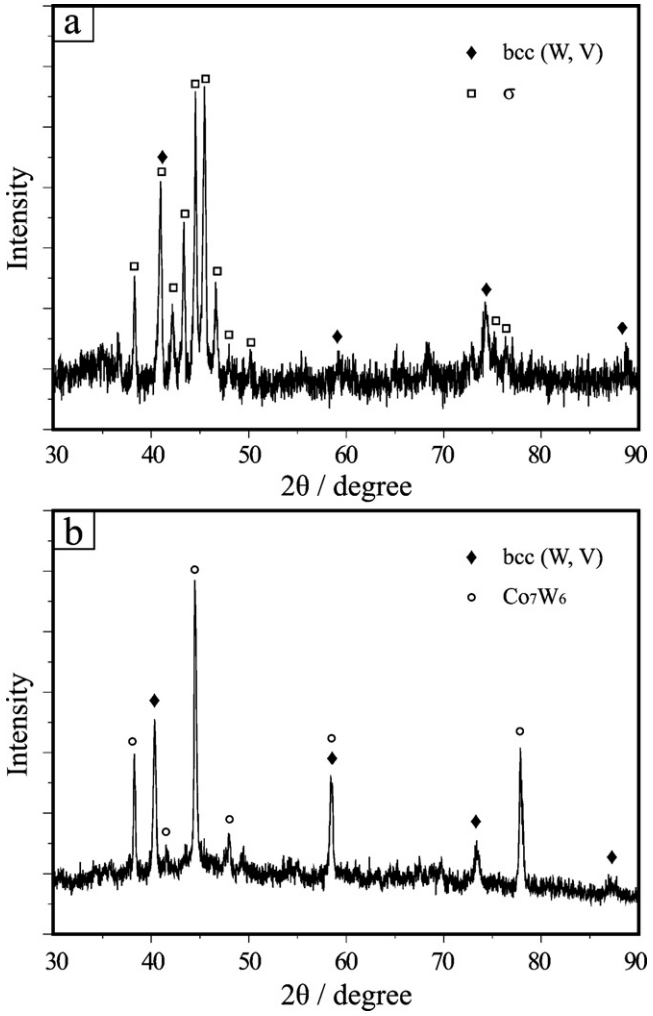


**Fig. 7.** X-ray diffraction patterns obtained from (a) the W-rich layer of the $Co_{25}W_{37}V_{38}$ (at. %) alloy annealed at 1100 °C for 5 weeks and (b) the W-rich layer of the $Co_{50}W_{15}V_{35}$ (at. %) alloy annealed at 1300 °C for 1 week.

### 3.3. Isothermal sections

The equilibrium compositions of the Co–W–V ternary system at 1100 °C, 1200 °C and 1300 °C determined by EPMA are listed in Tables 4–6, respectively.

**Table 4**
Equilibrium composition of the Co–W–V system at 1100 °C.

| Alloy (at. %) | Equilibria | Composition (at. %) | | | | | | | | |
|---|---|---|---|---|---|---|---|---|---|---|
| | Phase 1/phase 2/phase 3 | Phase 1 | | | Phase 2 | | | Phase 3 | | |
| | | Co | W | V | Co | W | V | Co | W | V |
| $Co_{25}W_{11.5}V_{63.5}$[a] | σ/bcc (W, V) | 29.8 | 6.3 | 63.9 | 2.9 | 45.3 | 51.8 | | | |
| $Co_{25}W_{22}V_{53}$[a] | σ/bcc (W, V) | 33.9 | 6.9 | 59.2 | 2.2 | 60.1 | 37.7 | | | |
| $Co_{25}W_{37}V_{38}$[a] | σ/bcc (W, V) | 37.8 | 7.3 | 54.9 | 1.6 | 70.2 | 28.2 | | | |
| $Co_{30}W_{21}V_{49}$[a] | σ/bcc (W, V) | 46.6 | 7.8 | 45.6 | 1.9 | 73.6 | 24.5 | | | |
| $Co_{50}W_{15}V_{35}$[a] | σ/$Co_7W_6$ | 55.2 | 7.1 | 37.7 | 49.5 | 24.5 | 26.0 | | | |
| $Co_{65}W_5V_{30}$ | σ/αCo | 60.4 | 6.5 | 33.1 | 69.1 | 3.1 | 27.8 | | | |
| $Co_{50}W_{31}V_{19}$[a] | αCo/$Co_7W_6$ | 71.2 | 3.7 | 25.1 | 51.1 | 31.5 | 17.4 | | | |
| $Co_{53}W_{37}V_{10}$[a] | αCo/$Co_7W_6$ | 77.9 | 6.4 | 15.7 | 53.9 | 38.1 | 8.0 | | | |
| $Co_{66}W_{29}V_5$ | αCo/$Co_7W_6$ | 83.0 | 9.4 | 7.6 | 56.7 | 40.2 | 3.1 | | | |
| $Co_{71}W_{26}V_3$ | αCo/$Co_7W_6$ | 84.6 | 10.9 | 4.5 | 57 | 41.5 | 1.5 | | | |
| $Co_{61}W_{11}V_{28}$ | αCo/$Co_7W_6$/σ | 70.4 | 3.1 | 26.5 | 51.7 | 27.6 | 20.7 | 60.7 | 6.9 | 32.4 |
| $Co_{53}W_{37}V_{10}$[a] | $Co_7W_6$/bcc (W, V) | 50.4 | 40.7 | 8.9 | 1.0 | 95.1 | 3.9 | | | |
| $Co_{50}W_{31}V_{19}$[a] | $Co_7W_6$/bcc (W, V) | 48.6 | 33.9 | 17.5 | 0.9 | 91.5 | 7.6 | | | |
| $Co_{50}W_{15}V_{35}$[a] | $Co_7W_6$/bcc (W, V) | 47.3 | 28.2 | 24.5 | 0.3 | 85.2 | 14.5 | | | |
| $Co_{50}W_{15}V_{35}$[a] | $Co_7W_6$/bcc (W, V)/σ | 47.2 | 26.2 | 26.6 | 0.5 | 81.8 | 17.7 | 51.2 | 7.8 | 41.0 |

[a] Alloys with separated morphology.

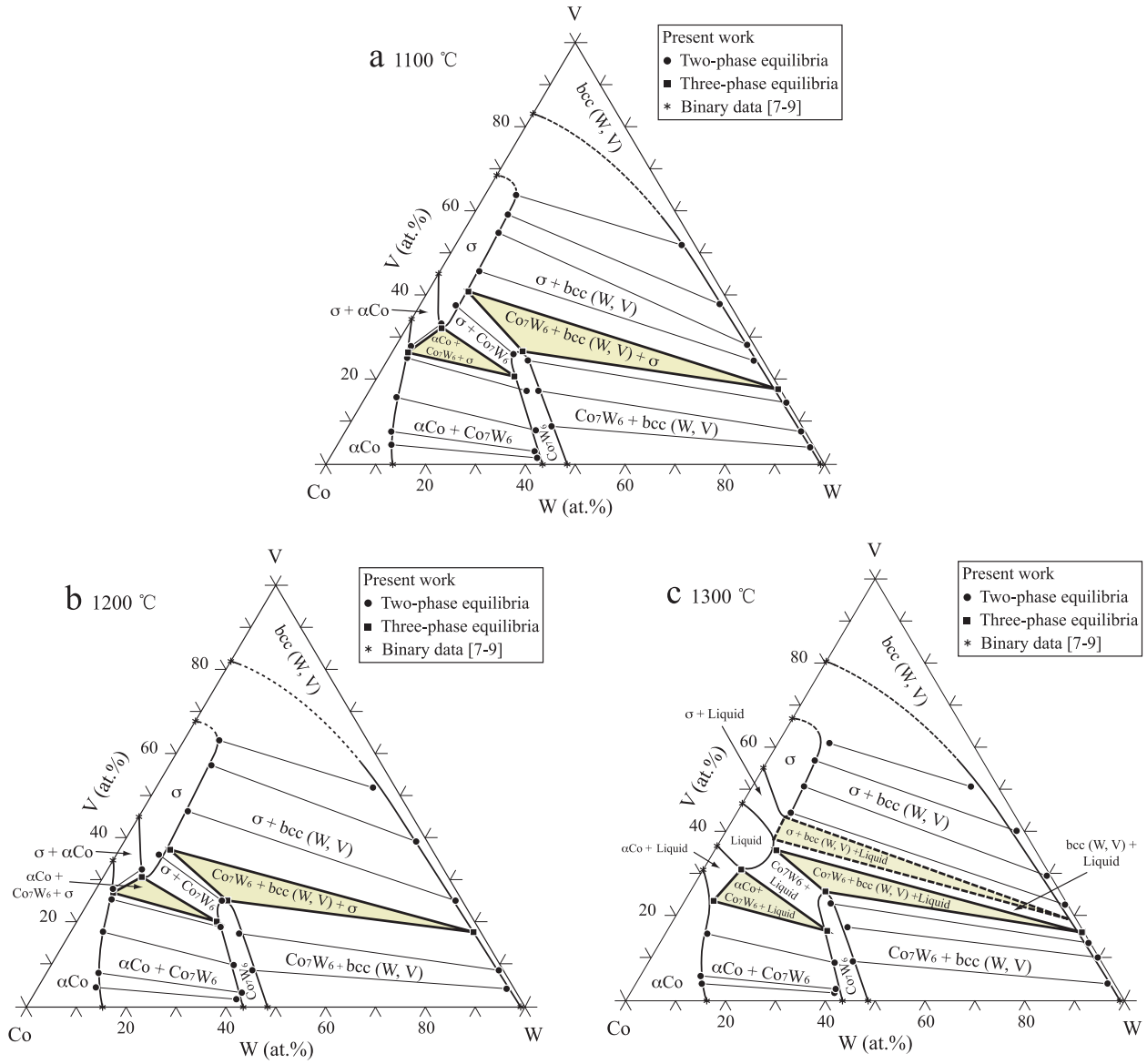


**Fig. 8.** Experimentally determined isothermal sections of the Co–W–V system at: (a) 1100 °C, (b) 1200 °C and (c) 1300 °C.

**Table 5**
Equilibrium composition of the Co–W–V system at 1200 °C.

| Alloy (at. %) | Equilibria | Composition (at. %) | | | | | | | | |
|---|---|---|---|---|---|---|---|---|---|---|
| | Phase 1/phase 2/phase 3 | Phase 1 | | | Phase 2 | | | Phase 3 | | |
| | | Co | W | V | Co | W | V | Co | W | V |
| $Co_{25}W_{11.5}V_{63.5}$[a] | σ/bcc (W, V) | 29.9 | 7.1 | 63.0 | 4.6 | 43.5 | 51.9 | | | |
| $Co_{25}W_{22}V_{53}$[a] | σ/bcc (W, V) | 34.4 | 8.3 | 57.3 | 2.5 | 58.5 | 39.0 | | | |
| $Co_{30}W_{21}V_{49}$[a] | σ/bcc (W, V) | 44.6 | 9.2 | 46.2 | 1.4 | 73.6 | 25.0 | | | |
| $Co_{50}W_{15}V_{35}$[a] | σ/$Co_7W_6$ | 55.6 | 8.4 | 36.0 | 48.4 | 26.5 | 25.1 | | | |
| $Co_{65}W_5V_{30}$ | σ/αCo | 60.5 | 6.8 | 32.7 | 68.8 | 3.3 | 27.9 | | | |
| $Co_{65}W_{10.5}V_{24.5}$ | αCo/$Co_7W_6$ | 70.3 | 4.3 | 25.4 | 51.7 | 29.5 | 18.8 | | | |
| $Co_{53}W_{37}V_{10}$[a] | αCo/$Co_7W_6$ | 75.8 | 6.7 | 17.5 | 53.5 | 36.7 | 9.8 | | | |
| $Co_{66}W_{29}V_5$ | αCo/$Co_7W_6$ | 81.7 | 10.4 | 7.9 | 55.2 | 41.6 | 3.2 | | | |
| $Co_{71}W_{26}V_3$ | αCo/$Co_7W_6$ | 83.8 | 11.8 | 4.4 | 57.2 | 41.1 | 1.7 | | | |
| $Co_{64}W_{8.5}V_{27.5}$ | αCo/$Co_7W_6$/σ | 69.3 | 3.8 | 26.9 | 51.8 | 28.0 | 20.2 | 61.5 | 7.8 | 30.7 |
| $Co_{53}W_{37}V_{10}$[a] | $Co_7W_6$/bcc (W, V) | 50.7 | 40.9 | 8.4 | 1.7 | 94.1 | 4.2 | | | |
| $Co_{50}W_{31}V_{19}$[a] | $Co_7W_6$/bcc (W, V) | 48.8 | 34.0 | 17.2 | 1.0 | 90.3 | 8.7 | | | |
| $Co_{50}W_{15}V_{35}$[a] | $Co_7W_6$/bcc (W, V)/σ | 47.2 | 27.6 | 25.2 | 1.5 | 80.8 | 17.7 | 52.8 | 9.9 | 37.3 |

[a] Alloys with separated morphology.

**Table 6**
Equilibrium composition of the Co–W–V system at 1300 °C.

| Alloy (at. %) | Equilibria | Composition (at. %) | | | | | | | | |
|---|---|---|---|---|---|---|---|---|---|---|
| | Phase 1/phase 2/phase 3 | Phase 1 | | | Phase 2 | | | Phase 3 | | |
| | | Co | W | V | Co | W | V | Co | W | V |
| $Co_{25}W_{11.5}V_{63.5}$[a] | σ/bcc (W, V) | 28.8 | 10.2 | 61.0 | 5.6 | 43.8 | 50.6 | | | |
| $Co_{25}W_{22}V_{53}$[a] | σ/bcc (W, V) | 33.9 | 9.3 | 56.8 | 1.6 | 58.3 | 40.1 | | | |
| $Co_{30}W_{21}V_{49}$[a] | σ/bcc (W, V) | 38.8 | 10.4 | 50.8 | 0.8 | 69.8 | 29.4 | | | |
| $Co_{33}W_{27}V_{40}$[a] | σ/bcc (W, V) | 44.7 | 11.0 | 44.3 | 0.6 | 76.7 | 22.7 | | | |
| $Co_{53}W_{37}V_{10}$[a] | αCo/$Co_7W_6$ | 76.0 | 8.3 | 15.7 | 53.9 | 37.2 | 8.9 | | | |
| $Co_{66}W_{29}V_5$ | αCo/$Co_7W_6$ | 82.1 | 12.2 | 5.7 | 56.6 | 40.7 | 2.7 | | | |
| $Co_{71}W_{26}V_3$ | αCo/$Co_7W_6$ | 82.9 | 13.1 | 4.0 | 57.3 | 41.1 | 1.6 | | | |
| $Co_{65}W_{10.5}V_{24.5}$ | αCo/$Co_7W_6$/liquid | 70.8 | 5.5 | 23.7 | 51.3 | 32.2 | 16.5 | 61.5 | 7.6 | 30.9 |
| $Co_{53}W_{37}V_{10}$[a] | $Co_7W_6$/bcc (W, V) | 49.9 | 41.0 | 9.1 | 1.43 | 94.5 | 4.07 | | | |
| $Co_{50}W_{31}V_{19}$[a] | $Co_7W_6$/bcc (W, V) | 46.9 | 35.7 | 17.4 | 0.4 | 89.6 | 10.0 | | | |
| $Co_{50}W_{15}V_{35}$[a] | $Co_7W_6$/bcc (W, V) | 47.6 | 29.4 | 23.0 | 0.3 | 86.0 | 13.7 | | | |
| $Co_{50}W_{15}V_{35}$[a] | $Co_7W_6$/bcc (W, V)/liquid | 47.2 | 26.9 | 25.9 | 0.4 | 83.4 | 16.2 | 52.2 | 12.0 | 35.8 |

[a] Alloys with separated morphology.

Based on the experimental data determined by this work, three isothermal sections at 1100 °C, 1200 °C and 1300 °C were constructed in Fig. 8(a)–(c). Fig. 8(a) shows the isothermal section at 1100 °C, where two three-phase regions (αCo + $Co_7W_6$ + σ and $Co_7W_6$ + bcc (W, V) + σ) and five two-phase regions (αCo + $Co_7W_6$, σ + αCo, σ + $Co_7W_6$, $Co_7W_6$ + bcc (W, V) and σ + bcc (W, V)) were determined in the present work. The $Co_7W_6$ phase is stabilized by the addition of V and the single phase region of the $Co_7W_6$ phase extends to the Co–V side, suggesting that V atoms substitute for W atoms. Therefore, the $Co_7W_6$ phase with the $D8_5$ structure can be designated as $Co_7(W, V)_6$, which is also in agreement with the chemical composition of constituent phases determined by EPMA. The maximum solubility of W in the σ phase is about 8 at. %. The isothermal section at 1200 °C, shown in Fig. 8(b), is quite similar to that at 1100 °C (Fig. 8(a)). Both of the maximum solubility of W in the σ phase (~9.5 at. %) and the maximum solubility of V in the $Co_7W_6$ phase (~25 at. %) are larger than those at 1100 °C. In the isothermal section at 1300 °C (Fig. 8(c)), the liquid phase was found to exist in the Co–V rich corner, which is in good agreement with that in the Co–V binary system [8]. It should be noted that the maximum solubility of W in the σ phase is about 11 at. %. The undetermined three-phase region (σ + bcc (W, V) + liquid) is shown in Fig. 8(c) in dashed lines.

## 4. Conclusions

(1) The as-cast $Co_{25}W_{11.5}V_{63.5}$, $Co_{25}W_{22}V_{53}$, $Co_{30}W_{21}V_{49}$, $Co_{50}W_{15}V_{35}$, $Co_{53}W_{37}V_{10}$, $Co_{50}W_{31}V_{19}$, $Co_{50}W_{15}V_{39}$ and $Co_{33}W_{27}V_{40}$ (at. %) alloys exhibit the top–bottom separated microscopic morphologies, suggesting that a stable liquid miscibility gap exists in the Co–W–V ternary system.
(2) Three isothermal sections of the Co–W–V ternary system at 1100 °C, 1200 °C and 1300 °C were experimentally determined and no ternary compound were found in this system. The $Co_7W_6$ and σ phases stabilized by the addition of V and W, respectively, were known.
(3) The firstly discovered phase separation phenomena and newly determined phase equilibria in the Co–W–V system will provide additional support for the thermodynamic assessment of this system and effective development of Co–W based alloys.

## Acknowledgements

This work was supported by the National Natural Science Foundation of China (Nos. 51031003 and 50971109) and the Ministry of Science and Technology of China (No. 2009DFA52170). The support from Fujian provincial Department of Science & Technology (Grant No. 2009I0024), Xiamen City Department of Science & Technology (Grant No. 3502Z0093001), and Aviation Science Fund (Grant No. 2009ZF68010) are also acknowledged.

## References

[1] R. Koc, S.K. Kodambaka, J. Eur. Ceram. Soc. 20 (2000) 1859–1869.
[2] S.G. Huang, L. Li, K. Vanmeensel, O. van der Biest, J. Vleugels, Int. J. Refract. Met. Hard Mater. 25 (2007) 417–422.
[3] N.G. Hashe, S. Norgren, H.-O. Andrén, J.H. Neethling, P.R. Berndt, Int. J. Refract. Met. Hard Mater. 27 (2009) 20–25.
[4] S.A. Cho, A. Hernandez, J. Ochoa, J. Lira-Olivares, Int. J. Refract. Met. Hard Mater. 15 (1997) 205–214.
[5] L.A. Dobrzański, W. Kasprzak, A. Zarychta, M. Ligarski, J. Mazurkiewicz, J. Mater. Process. Technol. 64 (1997) 93–99.
[6] H.K. Moon, K.B. Lee, H. Kwon, Mater. Sci. Eng. A: Struct. 474 (2008) 328–334.
[7] S.V. Nagender Naidu, A.M. Sriramamurthy, P. Rama Rao, J. Alloy Phase Diagrams 2 (1986) 43–52.
[8] J.F. Smith, Phase Diagrams Of Binary Vanadium Alloys, first ed., ASM International, Metals Park, OH, 1989, pp. 50–58.
[9] J.F. Smith, Phase Diagrams of Binary Vanadium Alloys, first ed., ASM International, Metals Park, OH, 1989, pp. 313–317.
[10] C.P. Wang, X.J. Liu, I. Ohnuma, R. Kainuma, K. Ishida, Science 297 (2002) 990–993.
[11] C.P. Wang, X.J. Liu, Y. Takaku, I. Ohnuma, R. Kainuma, K. Ishida, Metall. Mater. Trans. 35A (2004) 1243–1253.
[12] C.P. Wang, X.J. Liu, I. Ohnuma, R. Kainuma, K. Ishida, J. Mater. Res. 23 (2008) 933–940.